Proceedings of the 4th International Conference on Mathematical Physics and Computational Simulation
DOI: 10.54254/2753-8818/2026.34029

Study on Oxidation Mechanism of Molybdenum-Rhenium Alloy

Jiaying Wang*, Jinli Cao, Caifu Pan

China Institute of Atomic Energy, Beijing, China
wjy20017@163.com

Abstract. This study systematically investigates the high-temperature oxidation behavior and mechanism of Mo-7Re alloy at 1100 K in air. Through multi-scale characterization and first-principles calculations, it is found that the oxide layer exhibits a columnar grain structure, with holes and spalling pits formed on the surface due to the volatilization of MoO_3, resulting in reduced density. As fast channels for gas-phase diffusion of oxygen, holes jointly dominate oxygen transport together with lattice diffusion, while grain boundary diffusion makes a weak contribution. Precipitation of Re particles is observed inside the oxide layer. Calculations show that the solvation energy of oxygen in Mo (-0.08 eV) is much lower than that in Re (0.41 eV), and the formation energy of MoO_2 (-2.02 eV) is lower than that of ReO_2 (-1.71 eV). This confirms that Mo undergoes preferential oxidation, while Re enriches and precipitates in elemental form due to its repulsive interaction with oxygen. This study reveals the hole-diffusion coupling mechanism and the precipitation mechanism of Re, providing a theoretical basis for developing molybdenum-rhenium alloys with high-temperature oxidation resistance.

Keywords: Molybdenum-rhenium alloy, High-temperature oxidation, Oxidation mechanism, Rhenium precipitation

1. Introduction

Nuclear energy has been widely applied in various fields in recent years due to its high efficiency and environmental friendliness, including but not limited to civil power generation, medical and agricultural fields, and large marine power plants, playing an increasingly significant role in promoting global economic development [1]. After more than half a century of technological development, the key challenges facing the international nuclear energy field at present focus on improving fuel utilization efficiency, reducing radioactive waste emissions, realizing core miniaturization, and enhancing safety performance [2]. To meet these demands, new-generation nuclear reactor designs have been proposed successively, such as ultra-high temperature reactors, gas-cooled fast reactors, sodium-cooled fast reactors, and fusion reactors. Compared with conventional reactors, these advanced designs impose more stringent requirements on the performance of core materials, which need to withstand more extreme working temperatures, stronger radiation fields, and more severe corrosive conditions. Metallic molybdenum is regarded as an ideal candidate material for the structural components of the above-mentioned reactors due to its

© 2026 The Authors. This is an open access article distributed under the terms of the Creative Commons Attribution License 4.0 (https://creativecommons.org/licenses/by/4.0/).

DOI: 10.54254/2753-8818/2026.34029

ultra-high melting point of 2620 ℃, excellent mechanical strength maintained at high temperatures, and good chemical stability with alkaline media [3].

Despite its numerous advantages, molybdenum suffers from low-temperature brittleness (low room-temperature ductility), which leads to difficult processing and easy crack formation during welding or cold working, limiting its practical applications [4]. Solid solution strengthening is adopted to improve the processability of molybdenum, among which the doping effect of rhenium (Re) is the most significant. When the rhenium content reaches a certain proportion, the "rhenium effect" occurs [5], which significantly improves ductility, enhances high-temperature tensile strength and creep resistance, and optimizes weldability. This alloy was initially proposed by Soviet researchers as a candidate alloy for the fuel element cladding of the Bouk small fast neutron reactor [6]. In contemporary nuclear energy systems, advanced nuclear facilities such as the Idaho STAR gas-cooled reactor and the Japanese RAPID-L fast reactor have listed Mo-47.5Re alloy as the preferred material for core structural components and cooling system pipelines [7, 8].

However, the poor high-temperature oxidation resistance of such materials limits their further application in high-temperature aerobic environments. When common molybdenum alloy components work in aerobic environments above 750 ℃, a large amount of volatile oxides (such as MoO_3) will form rapidly [9-11]. The oxides formed on the molybdenum matrix, accompanied by accumulated shear strain during oxidation, accelerate the spalling of the surface oxide layer. This leads to rapid dimensional changes of molybdenum alloy components and even ablation and pulverization. Although extensive research has been conducted on molybdenum-rhenium alloys, key scientific issues remain to be elucidated in depth, such as the specific mechanism of the oxidation process, especially the diffusion path and action mechanism of oxygen in the alloy, as well as the behavior and influence of rhenium during oxidation. Taking Mo-7Re alloy as the research object, this study systematically investigates its oxidation behavior when exposed to air at 1100 K. By combining various characterization methods, it focuses on exploring the microstructural evolution of the oxide layer, oxygen diffusion mechanism, and distribution characteristics of rhenium. Combined with first-principles calculations, the microscopic behavior is explained from a thermodynamic perspective, aiming to reveal its oxidation mechanism and provide a theoretical basis for improving the high-temperature oxidation resistance of the alloy.

2. Experiments and calculations

2.1. Materials and experiments

Oxidation exposure of Mo-7Re alloy was carried out at 1100 K in air.

After oxidation, the surface morphology of the samples was observed using a Helios 5 CX field emission scanning electron microscope (SEM) equipped with a focused ion beam (FIB). FIB technology was used to prepare transmission electron microscope (TEM) samples of the cross-section of the oxide layer/substrate. The cross-sectional microstructure, phase composition, and element distribution were analyzed using a Themis Z aberration-corrected transmission electron microscope equipped with an energy dispersive X-ray spectrometer (EDS). An ON-6801 oxygen-nitrogen analyzer was used to determine the oxygen content in the unoxidized substrate of the samples.

DOI: 10.54254/2753-8818/2026.34029

2.2. Calculation methods and models

In this study, calculations were performed using the Vienna Ab-initio Simulation Package (VASP) based on density functional theory (DFT) and plane-wave pseudopotentials [12-14]. The projector augmented-wave (PAW) method was applied to describe electron-ion interactions [15], and the PBE functional within the generalized gradient approximation (GGA) was used to handle electron-electron exchange-correlation effects [16]. The plane-wave cutoff energy was set to 400 eV, and the convergence criterion for ionic relaxation in the supercell was 1×10^{-5} eV.

The solvation energy of oxygen atoms in molybdenum and rhenium can be expressed as:

$$E_O^f(Mo) = E(Mo_{128}O) - E(Mo_{128}) - \mu_O \tag{1}$$

$$E_O^f(Re) = E(Re_{54}O) - E(Re_{54}) - \mu_O \tag{2}$$

where $E(Mo_{128}O)$, $E(Re_{54}O)$, $E(Mo_{128})$,and $E(Re_{54})$ are the total energies of Mo with interstitial oxygen, Re with interstitial oxygen, and defect-free Mo and Re supercells, respectively. The chemical potential of oxygen μ_O is half the energy of an oxygen molecule, i.e., -4.90 eV.

3. Results and discussion

3.1. Morphology and characteristics of the oxide layer

Figure 1 shows the SEM images of the surface morphology of the molybdenum-rhenium alloy after high-temperature oxidation. Figure 1(a) reveals that fine oxide particles form on the sample surface, which are composed of vertically grown columnar grains with clear surface contours and obvious gaps between grains. Further analysis of the microstructure in local regions via high-resolution imaging (Figure 1(b)) shows that protrusions, depressions, and holes are distributed on the particle surface, indicating local volatilization. This is likely caused by the volatilization of MoO_3 at high temperatures, which induces cracking of the oxide layer and the formation of spalling pits in local areas.

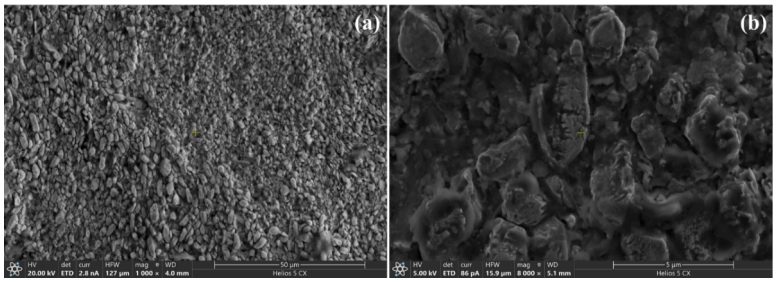

Figure 1. (a) Low-magnification overall morphology and (b) high-magnification local details of the alloy after oxidation

For the oxidized molybdenum-rhenium alloy sample, FIB technology was used to extract thin sections required for TEM analysis from the oxidized surface. The sampling direction is shown in Figure 2, with sampling conducted vertically to the oxidized surface along the depth direction. The

DOI: 10.54254/2753-8818/2026.34029

cross-sectional TEM image of the microstructure is presented in Figure 3(a), which shows a distinct layered structure in the sample cross-section: the upper part is a dark gray region, and the lower part is a light gray region, separated by a clear interface. Further observation via magnification of region B near the interface (Figure 3(b)) and EDS mapping (Figures 3(c)-(e)) reveals the element distribution characteristics: oxygen is highly concentrated in the dark gray region, while the proportions of Mo and Re are significantly higher in the light gray region. Based on compositional and morphological analysis, the upper dark gray region is identified as the oxide layer with a thickness of approximately 8.53 μm, and the lower light gray region is the unoxidized alloy substrate. In terms of crystal structure, the oxide layer exhibits a typical columnar grain morphology with grains growing directionally along specific crystallographic directions; the substrate region consists of equiaxed grains with relatively uniform grain size and a complete, undistorted grain boundary network. Holes of varying sizes are distributed in the oxide layer (indicated by arrows in Figure 3(b)), mostly oval or irregular in shape, with some distributed along grain boundaries. No holes are observed in the substrate, which has a complete and continuous grain boundary structure, reflecting the good density of the unoxidized alloy substrate.

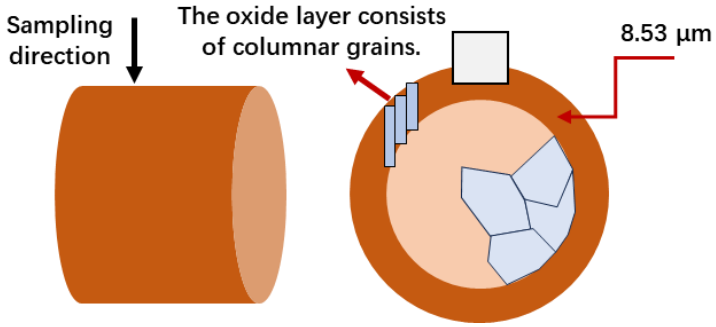

Figure 2. FIB sampling direction and grain morphology of the oxide layer and substrate layer

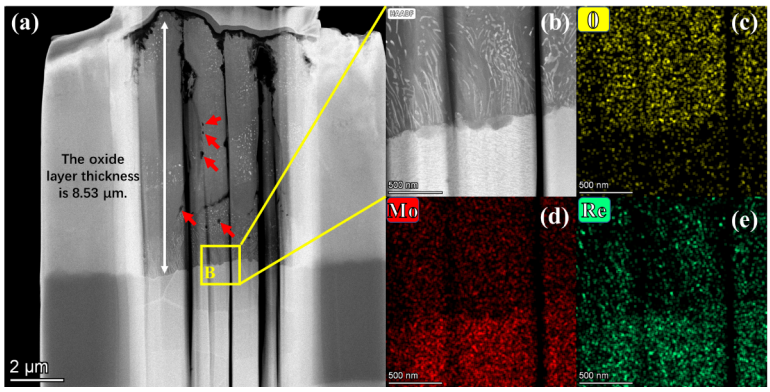

Figure 3. (a) Cross-sectional TEM image of the alloy after oxidation, (b) enlarged image of frame B in (a), (c)~(e) corresponding EDS maps of different elements distributed in (b)

3.2. Diffusion path of oxygen

To further analyze the diffusion behavior of oxygen, high-resolution electron microscopy combined with energy dispersive X-ray spectroscopy (EDS) line scanning was used to quantitatively characterize the distribution of oxygen across grain boundaries in the oxide layer and substrate. Figure 4 shows the HAADF images at grain boundaries and three selected line scanning paths

DOI: 10.54254/2753-8818/2026.34029

(indicated by yellow arrows), where (a) corresponds to the grain boundary region of the oxide layer, and (b) and (c) correspond to the grain boundary regions of the substrate. The paths are set perpendicular to the grain boundaries and pass through the interior of adjacent grains. The oxygen content distribution curves along the three paths in Figure 4(d) show that no significant increase or sharp peak in oxygen content is observed at the grain boundaries along the three scanning paths. The intensity fluctuation near grain boundaries is consistent with that inside grains. This indicates that grain boundary diffusion is not the dominant mechanism for rapid oxygen diffusion under the experimental conditions.

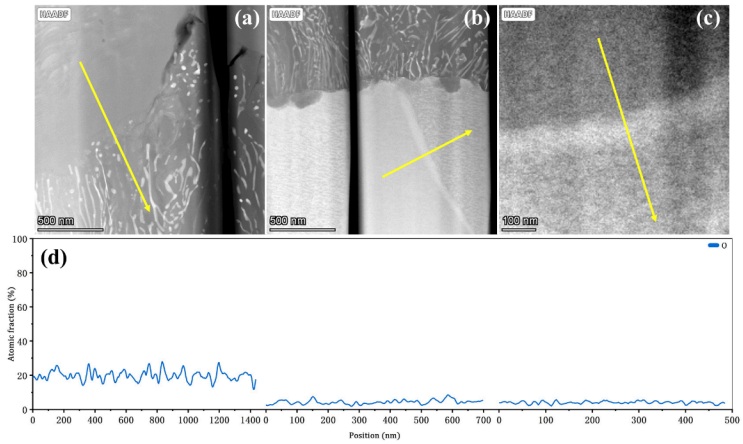

Figure 4. Linear oxygen distribution across grain boundaries in the oxide layer and substrate, (a) at the grain boundary of the oxide layer, (b) at the grain boundary of the substrate, (c) at the grain boundary of the substrate, (d) O content profiles corresponding one-to-one to the line scans in (a)~(c)

Combined with the observation of numerous holes in the oxide layer (Figure 3), this study concludes that oxygen diffusion is jointly determined by lattice (bulk) diffusion and gas-phase diffusion (direct penetration of oxygen through holes). First, the matrix metal Mo undergoes staged oxidation reactions: the initially formed thermodynamically stable phase MoO_2 is gradually oxidized to MoO_3 with prolonged oxidation time. MoO_3 continuously volatilizes at high temperatures (>773 K), leading to the formation and proliferation of holes in the oxide layer. These nanoscale holes not only disrupt the continuity of the oxide layer but also construct gas-phase diffusion channels on the surface. This hole-diffusion coupling effect not only accelerates the longitudinal transport of oxygen into the oxide layer but also induces interfacial stress concentration by weakening the bonding strength between the oxide layer and the substrate, ultimately resulting in the degradation of the protective performance of the oxide film and the formation of spalling pits (Figure 1(b)). Although grain boundary diffusion cannot be completely ruled out, its relative contribution in this system is negligible and does not lead to observable oxygen enrichment at grain boundaries.

The oxygen content near the substrate grain boundaries in Figure 4 was measured by EDS, with the sum of oxygen and other element contents normalized. To accurately measure the oxygen content in the substrate, an ON-6801 oxygen-nitrogen analyzer was used, and the results are shown in Table 1. A standard sample with an oxygen content of 0.097% was measured to be 0.098%, indicating a relative error of approximately 1.03% in the measurement results, with a small deviation from the standard value and high accuracy. The measured oxygen content in the unoxidized MoRe alloy substrate is close to 0%, indicating that oxygen mainly diffuses into the alloy from the outside during oxidation.

DOI: 10.54254/2753-8818/2026.34029

Table 1. Mass percentage of oxygen content in standard samples and MoRe substrate

Sample	Oxygen Content (%)	Weight (g)
Standard sample 0.097	0.098	0.1106
MoRe substrate 1	0.00147	0.1302
MoRe substrate 2	0.00159	0.1336

3.3. Behavior of rhenium during oxidation

During TEM characterization of the oxide layer microstructure, a large number of white bright spots with high contrast were observed randomly distributed inside the oxide layer (Figure 5), while no similar features were found in the unoxidized metal substrate, indicating that this is a unique phenomenon during oxidation. These bright spots are not enriched on the surface or grain boundaries of the oxide layer but are randomly distributed within it. Multi-scale analysis of the marked region (Area #1) and EDS mapping results (Figure 5) show significant segregation of rhenium (Re) in these bright spot regions. Combined with quantitative point EDS analysis (Table 2), the oxygen content (~9.84 at%) in these regions is significantly lower than that of the surrounding Mo- and O-rich oxide matrix, while the Re content (~64.89 at%) is much higher than that in the alloy substrate. To clarify the phase composition of the white bright spots, high-angle annular dark-field (HAADF) imaging and selected-area inverse FFT analysis were performed on typical target particles (Figure 6). The diffraction spots in Figure 6(b) exhibit the characteristics of a typical hexagonal close-packed (hcp) structure, identified as the diffraction pattern of the [111] zone axis of Re. A comparison with the standard diffraction pattern of metallic Re (Figure 6(c)) shows complete consistency in spot positions and symmetry. Combined with EDS compositional analysis of this region, the white bright spots are finally identified as elemental metallic rhenium (Re) particles.

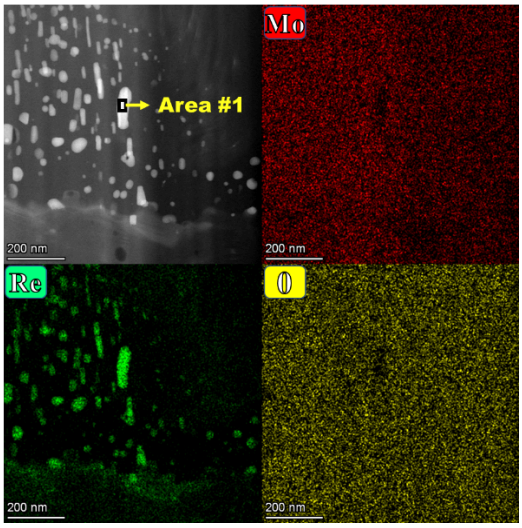

Figure 5. EDS area scan results of white bright spots in the oxide layer

DOI: 10.54254/2753-8818/2026.34029

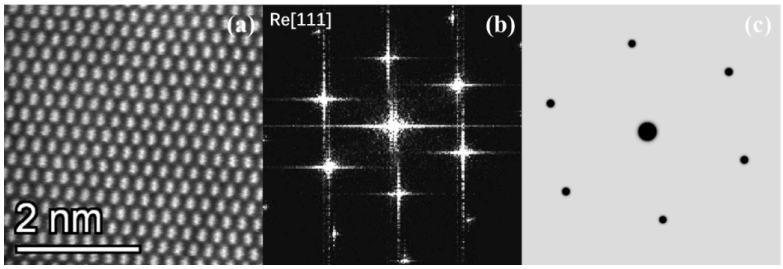

Figure 6. Phase identification results of Re-rich regions in the oxide layer (a) High-angle annular dark-field (HAADF) image of the white bright spot region, (b) inverse FFT analysis pattern of the selected area in (a), (c) diffraction calibration of the [111] zone axis of standard metallic rhenium (Re)

Table 2. Elemental content in Area #1

Element	Atomic Percentage (%)	Error (%)
O	9.84	5.34
Mo	25.27	7.25
Re	64.89	7.50

3.4. First-principles calculation results

To further clarify the precipitation behavior of Re, first-principles calculations were conducted in this study to systematically analyze the occupancy tendency of oxygen atoms in molybdenum-rhenium alloy and its effect on Re segregation from a thermodynamic perspective. Due to the small atomic radius of oxygen, it tends to occupy lattice interstitial sites. In the modeling process, oxygen atoms were placed at tetrahedral interstitial sites (TIS) and octahedral interstitial sites (OIS) for energy calculation, as schematically shown in Figure 7. The calculation results (Figure 8(b)) show that oxygen atoms are more stably located at TIS in both Mo and Re, which is consistent with previous literature reports [17]. According to Equations (1) and (2), the solvation energy of oxygen in Mo is -0.08 eV, while that in Re is 0.41 eV, indicating that oxygen has a higher solubility in Mo and is more prone to react with Mo. Furthermore, the formation energy of molybdenum dioxide (MoO_2) is -2.02 eV [18], lower than that of rhenium dioxide (ReO_2) (-1.71 eV) [19], thermodynamically confirming that Mo is more susceptible to oxidation to form molybdenum dioxide. As reported in the literature [17], the binding energy between O and Re in Mo is negative, indicating a repulsive interaction between them. As oxidation proceeds, the oxide layer thickens continuously and Mo is consumed, leading to an increase in local Re concentration. Due to the difficulty of Re oxidation and its thermodynamic repulsion with O, Re gradually enriches and eventually precipitates as nanoscale metallic particles inside the oxide layer, as schematically illustrated in Figure 8(a).

DOI: 10.54254/2753-8818/2026.34029

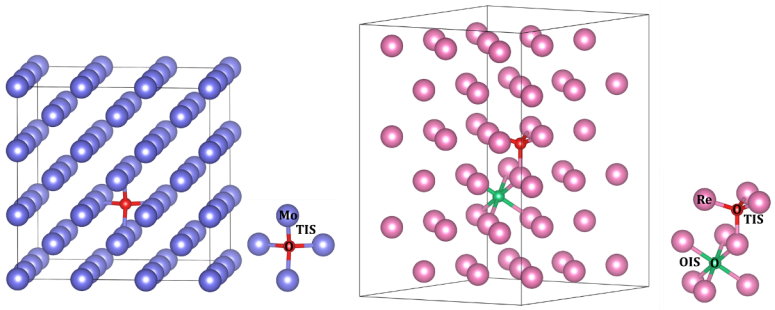

Figure 7. Structures of interstitial sites in rhenium and molybdenum, where small blue balls represent Re, small pink balls represent Mo, small red balls represent O at TIS, and small green balls represent O at OIS

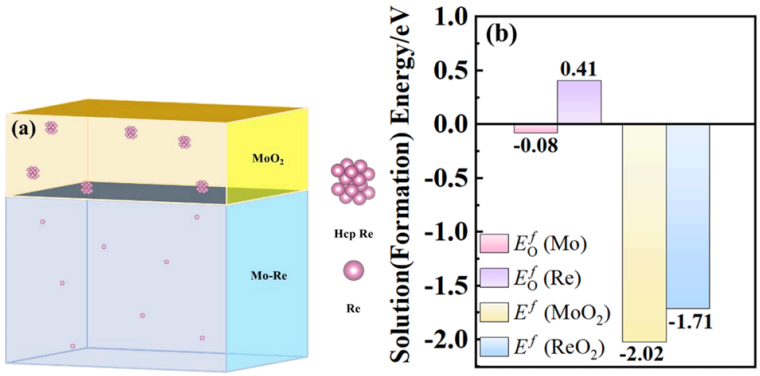

Figure 8. (a) Overall schematic diagram, where the yellow region represents the oxide layer MoO_2 with pink clusters (hcp-structured Re particles), the blue region represents the Mo-7Re solid solution, and pink atoms represent Re atoms; (b) dissolution energy of O in Mo and Re, and formation energy of MoO_2 [18] and ReO_2 [19]

4. Conclusions

Combining experimental characterization and first-principles calculations, this study thoroughly reveals the oxidation mechanism of Mo-7Re alloy exposed to air at 1100 K, and the main conclusions are as follows:

1. Structure and characteristics of the oxide layer: After oxidation, the alloy forms a MoO_2/MoO_3 oxide layer dominated by columnar grains with a thickness of approximately 8.53 μm. A large number of holes generated by the volatilization of MoO_3 exist inside the oxide layer, which disrupt the density and continuity of the oxide layer.

2. Diffusion path of oxygen: EDS line scanning analysis shows no significant oxygen enrichment at grain boundaries, proving that grain boundary diffusion is not the main pathway for oxygen transport under the experimental conditions. Oxygen diffusion is jointly dominated by lattice bulk diffusion and gas-phase diffusion through the hole network. This hole-diffusion coupling mechanism greatly accelerates the inward transport of oxygen and the outward volatilization of oxidation products, leading to the failure of the protective performance of the oxide layer and triggering spalling.

3. Oxidation behavior of rhenium: Nanoscale elemental metallic rhenium particles are found inside the oxide layer. First-principles calculations explain this phenomenon from a thermodynamic

DOI: 10.54254/2753-8818/2026.34029

perspective: the solvation energy of oxygen in molybdenum is much lower than that in rhenium, resulting in preferential reaction of oxygen with molybdenum. Additionally, the formation energy of MoO_2 is lower than that of ReO_2, confirming that Mo is thermodynamically far more prone to oxidation than Re. Rhenium gradually enriches due to its difficulty in oxidation and mutual repulsion with oxygen, eventually forming nanoscale metallic rhenium particles.

In summary, the high-temperature oxidation of Mo-7Re alloy is a complex process involving the porosity of the oxide layer caused by volatile oxides, subsequent coupled transport of rapid gas-phase/bulk diffusion of oxygen, and thermodynamically driven precipitation of rhenium. Future strategies to improve the high-temperature oxidation resistance of the alloy should focus on inhibiting the formation of volatile oxides to maintain the density of the oxide layer, or modifying the oxide layer structure to hinder rhenium precipitation and rapid oxygen transport.

References

[1] Wolfgang H. Materials for Nuclear Plants. 2nd Ed. Transl by Shanghai Nuclear Engineering Research and Design Institute. Shanghai: Shanghai Science and Technology Press, 2017

[2] Yang J, Yang Z C, Xu L J, et al. Review of 2017 nuclear energy technology hotspots. Sci Technol Rev, 2018, 36(1): 31.

[3] Busby J T, Leonard K J. Space fission reactor structural materials: Choices past, present, and future. JOM, 2007, 59(4): 20.

[4] Hu BL, Ge SW, Han JY, et al. ZrTiO4 secondary phase effects on ductility and toughness of molybdenum alloys. Mater Lett 2022; 307: 131077.

[5] Geach GA, Hughes JE. In: Benesovsky F, editor. The alloys of Rhenium with Molybdenum or with Tungsten and having good high temperature properties, 2nd Plan see Seminar. London: Pergamon; 1956.

[6] Zinkle S J, Ott L J, Ingersoll D T, et, al. Over-view of materials technologies for space nuclear power and propulsion [C]. AIP Conference Proceedings. 2002, 608: 1063-1069.

[7] Jahshan S N, Borkowski J A. A modular gascoolsed cermet reactor system for plantary base power [J]. Symposium Space Nuclear Power & Propulsion. 1993, 1: 641.

[8] Kambe M, Tsunoda H, Mishia K, et al. Rapid – L operator – free fast reactor concept without any control rods [J]. Nuclear Technology, 2003, 1: 11.

[9] D. Glass, Ceramic Matrix Composite (CMC) Thermal Protection Systems (TPS) and Hot Structures for Hypersonic Vehicles, 15th A｜AA International Space Planes and Hypersonic Systems and Technologies Conference, 2008 2008–2682.

[10] T.A. Parthasarathy, M.G. Mendiratta, D.M. Dimiduk, Oxidation mechanisms in Mo reinforced Mo5SiB2(T2)–Mo3Si alloys, Acta Mater. 50 (2002) 1857–1868.

[11] S.P. Chakraborty, S. Banerjee, I.G. Sharma, A.K. Suri, Development of silicide coating over molybdenum based refractory alloy and its characterization, J. Nucl. Mater. 403 (2010) 152–159.

[12] G. Kresse, J. Hafner, Ab initio molecular dynamics for liquid metals, Phys. Rev. B 47 (1993) 558–561.

[13] G. Kresse, J. Furthmüller, Efficiency of ab-initio total energy calculations for metals and semiconductors using a plane-wave basis set, Comput. Mater. Sci. 6 (1) (1996) 15–50.

[14] G. Kresse, J. Furthmüller, Efficient iterative schemes for ab initio total-energy calculations using a plane-wave basis set, Phys. Rev. b. 54 (1996) 11169–11186.

[15] P.E. Blochl, Projector augmented-wave method, Phys, Rev. B 50 (1994) 17953–17979.

[16] J.P. Perdew, J.A. Chevary, S.H. Vosko, K.A. Jackson, M.R. Pederson, D.J. Singh, C. Fiolhais, Atoms, molecules, solids, and surfaces: Applications of the generalized gradient approximation for exchange and correlation, Phys. Rev. B. 46 (11) (1992) 6671–6687.

[17] Pan C , Cao J , He X , et al. The trapping effect of transitional metals on oxygen in Mo from first-principles calculations [J].Computational Materials Science, 2024, 239112986.

[18] Amanda W , Ryan K , Matthew M , et al.A framework for quantifying uncertainty in DFT energy corrections. [J]. Scientific reports, 2021, 11 (1): 15496-15496.

[19] A A E , Chris W .High-throughput DFT calculations of formation energy, stability and oxygen vacancy formation energy of ABO3 perovskites. [J]. Scientific data, 2017, 4(1): 170153.